A pseudo-elastic local meshless method for analysis of material nonlinear problems in solids

Y. T. Gu[1,2 *], Q. X. Wang[1], K. Y. Lam[3], and K. Y. Dai[4]

[1] School of Aerospace, Mechanical & Mechatronic Engineering, J07
University of Sydney, NSW, 2006, Australia

[2]School of Engineering System, Queensland University of Technology,
GPO Box 2434, Brisbane, QLD 4001,Australia

[3] Institute of High Performance Computing, 1 Science Park Road, #01-01 The Capricorn,
Singapore Science Park II, Singapore 117528

[4] Department of Mechanical Engineering, National University of Singapore,
10 Kent Ridge Crescent, Singapore 119260

Abstract

This paper aims to develop an effective meshless technique for the analysis of elasto-plastic problems. The material nonlinearity will be studied by a new pseudo-elastic local radial point interpolation formulation which is based on the local Petrov-Galerkin form and the radial basis function (RBF) interpolation. Hencky's total deformation theory is used to define the effective Young's modulus and Poisson's ratio, which are treated as spatial field variables, and considered as functions of the final stress state and material properties. These effective material parameters are obtained in an iterative manner using the strain controlled projection method. Several numerical examples are presented to illustrate the effectivity of the newly developed formulation, and the numerical results obtained by the present method closely agree with the results obtained by other methods. It has proven that the present pseudo-elastic local meshless method is effective and easy to apply to the analysis of elasto-plastic materials subjected to proportional loading

Keywords: Numerical simulation, Material nonlinearity, Elasto-plastic analysis, Meshless method, RBF, Local weak-form

[*] Corresponding author: yuantong.gu@aeromech.usyd.edu.au;
Tel.: +61-2-93512284; Fax: +61-2-93517060

1. Introduction

To understand the material behaviour in the plastic range is essential for the analysis and design of engineering structures. However, the nonlinear stress-strain relationship and the loading path dependency in the plastic range make the analysis tedious. In recent times, the finite element method (FEM) has become a dominated numerical simulation tool for the analysis of material behaviour in the elastic and elasto-plastic ranges, especially in practical engineering applications [1][2]. Moreover, because of the rapid development of engineering and science, the problems of material nonlinearity have become even more challenging. In addition, some shortcomings of FEM have been revealed because of the use of meshes and elements [3]. To overcome these shortcomings, the concept of meshless method has been proposed [3][4].

In recent years, some meshless methods have achieved remarkable progress. According to using or not using integration, meshless methods can be largely grouped into two different categories [4]: 1) the meshless method based on strong-forms of partial differential equations (PDEs), and 2) the meshless method based on weak-forms of PDEs. The first category includes the smooth particle hydrodynamics (SPH) [5], the meshless collocation method [6][7], etc. The second category includes the diffuse element method [8], the element-free Galerkin (EFG) method [9], the reproducing kernel particle method (RKPM) [10], the point interpolation method (PIM) [11], meshless boundary-type methods[12][13], the meshless local Petrov-Galerkin (MLPG) method [14]-[16], etc. In the second category, some methods are based on the global Galerkin weak-form (e.g., EFG), and some are based on the local weak-forms (e.g., MLPG).

In order to alleviate the global background cells for the numerical integration, Atluri and Zhu [14] proposed the MLPG, in which the local Petrov-Galerkin weak-form and the moving least squares approximation (MLSA) were used. Following the idea of the MLPG

method, Liu and Gu [18][19] developed the local radial point interpolation method (LRPIM) based on the locally weighted residual method and the radial basis function (RBF) interpolation. The LRPIM method has some advantages compared with the meshless methods based on the global weak-forms (e.g., the EFG method). Firstly, it does not need a global mesh for either function approximation or integration, and only local integrations over simply-shaped local domains are needed for most of the internal nodes. Secondly, the implementation procedure of LRPIM is very similar to the methods based on strong-forms or the collocation method [4]. Thirdly, the RBF interpolation used in LRPIM is robust, accurate and easy to extend to three-dimensional (3-D) problems. In addition, the boundary conditions can be easily and accurately enforced due to the Kronecker delta function properties of RBF shape functions. Hence, LRPIM has been successfully applied to many problems including two-dimensional (2-D) elasto-static and dynamic analyses of solids[18], 4th order ordinary differential equations (ODEs) or partial differential equations(PDEs) for beam structures [17], the 2-D contact problems [20][21], microelectronic mechanical systems (MEMS)[22], and so on. However, the current publications of LRPIM for solids and structures are limited to linear elasticity. Although there are some related researches for the strong-form methods [23][24], no research for the material nonlinear analysis by the local weak-form meshless method, e.g., LRPIM, has been reported,.

A group of numerical techniques have been developed so far to solve the elasto-plastic problems. Marcal and King [25] developed a stiffness method, in which they used the incremental stress-strain relationship based on the partial stiffness coefficient. Owen and Hinton[26] provided finite element computer implementation of elasto-plastic problems based on incremental theory. Seshadri [27] developed a GLOSS method based on two-linear elastic finite element analysis which is used to evaluate the approximate plastic strains at certain local regions. Babu and Iyer [28] developed a robust method using relaxation method,

which is based on GLOSS method of analysis, and an attempt was made to satisfy force equilibrium in the plastic range. Desikn and Sethuraman [29] developed a so-called pseudo-elastic method for the determination of inelastic material parameters. In their method, the material parameters were considered as field variables, and the linear elastic finite element analysis was carried out to get the pseudo-stress distributions. The three algorithms, the projection method, the arc-length method, and the Neuber rule, were used to calculate the effective material parameters, in which the strain controlled projection method is very straightforward and easy to use. This pseudo-elastic method is very simple to use, and is very applicable for material nonlinear problems with a proportional loading. Hence, the pseudo-elastic method will be applied in this paper.

In this paper, a meshless pseudo-elastic LRPIM formulation is developed for solving elasto-plastic problems. The locally weighted residual method is used to get the meshless system of equations and the radial basis interpolation is applied to construct the meshless shape functions. The Hencky's total deformation theory is used to define effective material parameters, which are treated as spatial field variables and considered to be functions of final state of equilibrium stress and material properties. These effective material parameters are obtained in an iterative manner using strain controlled projection method and the meshless pseudo-elastic analyses. Examples are presented to illustrate the effectivity of the newly developed formulation for the elasto-plastic analysis through comparing the numerical results with those obtained by other methods.

2. LRPIM formulation

2.1 Construction of the RBF meshless shape function

There are a number of ways to construct meshless shape functions [4]. In this paper, the radial basis function (RBF) interpolation is used to construct the meshless shape functions,

because it is stable and accurate [3]. The locally supported RBF interpolation formulation can be written as:

$$u(\mathbf{x}) = \sum_{i=1}^{n} R_i(r) a_i + \sum_{j=1}^{m} p_j(\mathbf{x}) b_j = \mathbf{R}^T \mathbf{a} + \mathbf{B}^T \mathbf{b} = \{\mathbf{R} \quad \mathbf{B}\} \begin{Bmatrix} \mathbf{a} \\ \mathbf{b} \end{Bmatrix} \tag{1}$$

where $R_i(r)$ is the RBF, n is the number of nodes in the interpolation domain of the interpolation point $\mathbf{x}$, $p_j(\mathbf{x})$ is monomials in the space coordinates $\mathbf{x}^{\mathrm{T}}=[x,y]$, m is the number of polynomial basis functions, and coefficients a_i and b_j are interpolation constants. The unique variable in a RBF is the distance, r, between the interpolation point $\mathbf{x}$ and a field node $\mathbf{x}_i$, and it makes the RBF interpolation easily extend to three-dimensional problems.

There are a number of RBFs, and their characteristics in meshless methods have been widely investigated [3]. In this paper, the locally supported multi-quadrics (MQ) RBF is used to construct the meshless shape function based on the local interpolation domains, which is written as

$$R_i(\mathbf{x}) = [r_i^2 + (\alpha_0 d_i)^2]^q \tag{2}$$

where α_0 is a dimensionless coefficient, and d_i is a parameter of the nodal spacing. The selections of two parameters (α_0 and q) will significantly influence the performance of MQ RBF. The effects of α_0 and q have been studied in details in many publications [3][4]. It has been found that α_0=1.0 and q=1.03 lead to good results for most problems in solids, and therefore, these values will be used in this paper.

It should be mentioned that the MQ RBF usually can lead to accurate and convergent results for most problems in solids. However, there are still some technical issues in the use of MQ RBF. Firstly, there is still not a theoretical method to determine the optimal values of two parameters in MQ: α_0 and q. Secondly, MQ RBF can be the ill-conditioned, especially for a larger scale. To overcome the ill-conditioning problem, we used the MQ RBF interpolation locally (i.e. based on a local interpolation domain), and the normalization is

also applied. In addition, the number of field nodes selected in the interpolation domain is controlled. In a word, we limit the interpolation in a small scaled local domain.

Coefficients a_i and b_i in Equation (1) can be solved by enforcing Equation (1) to be satisfied at the n nodes surrounding a point $\mathbf{x}$. Then, Equation (1) can be re-written in matrix form as follows

$$\begin{Bmatrix} \mathbf{u}_e \\ \mathbf{0} \end{Bmatrix} = \begin{bmatrix} \mathbf{R}_0 & \mathbf{B}_m \\ \mathbf{B}_m^{\mathrm{T}} & \mathbf{0} \end{bmatrix} \begin{Bmatrix} \mathbf{a} \\ \mathbf{b} \end{Bmatrix} = \mathbf{G}\mathbf{a}_0 \tag{3}$$

where

$$\mathbf{B}_m^{\mathrm{T}} = \begin{bmatrix} p_1(\mathbf{x}_1) & p_1(\mathbf{x}_2) & \cdots & p_1(\mathbf{x}_n) \\ p_2(\mathbf{x}_1) & p_2(\mathbf{x}_2) & \cdots & p_2(\mathbf{x}_n) \\ \vdots & \vdots & \ddots & \vdots \\ p_m(\mathbf{x}_1) & p_m(\mathbf{x}_2) & \cdots & p_m(\mathbf{x}_n) \end{bmatrix}, \quad \mathbf{R}_0 = \begin{bmatrix} R_1(r_1) & R_2(r_1) & \cdots & R_n(r_1) \\ R_1(r_2) & R_2(r_2) & \cdots & R_n(r_2) \\ \cdots & \cdots & \cdots & \cdots \\ R_1(r_n) & R_2(r_n) & \cdots & R_n(r_n) \end{bmatrix} \tag{4}$$

Solving coefficients $\mathbf{a}_0$ from Equation (3) and substituting them back into Equation (1), the following RBF interpolation formulation is then obtained

$$u(\mathbf{x}) = \begin{Bmatrix} \mathbf{R} & \mathbf{B} \end{Bmatrix} \mathbf{G}^{-1} \begin{Bmatrix} \mathbf{u}_e \\ \mathbf{0} \end{Bmatrix} = \begin{Bmatrix} \mathbf{\Phi}(\mathbf{x}) & \mathbf{\Lambda}(\mathbf{x}) \end{Bmatrix} \begin{Bmatrix} \mathbf{u}_e \\ \mathbf{0} \end{Bmatrix} \tag{5}$$

where the RBF shape function $\mathbf{\Phi}(\mathbf{x})$ is defined by

$$\mathbf{\Phi}(\mathbf{x}) = [\phi_1(\mathbf{x}), \phi_2(\mathbf{x}), ..., \phi_n(\mathbf{x})] = \left(\begin{Bmatrix} \mathbf{R} & \mathbf{B} \end{Bmatrix} \mathbf{G}^{-1} \right)\Big|_{1-n} \tag{6}$$

where $\mathbf{\Phi}(\mathbf{x})$ is a vector which includes $1 - n$ elements of $\begin{Bmatrix} \mathbf{R} & \mathbf{B} \end{Bmatrix} \mathbf{G}^{-1}$.

It has been proven that the RBF shape functions, given in Equation (6), satisfy the Kronecker delta condition [4], which makes it easy to enforce the boundary conditions in the meshless method based on the RBF shape functions.

2.2 The local weak-form and the meshless discretization

Consider the following two-dimensional solid problem in the domain Ω bounded by Γ:

$$\sigma_{ij,j} + b_i = 0 \quad \text{in} \quad \Omega \tag{7}$$

where σ_{ij} is the stress tensor corresponding to the displacement field u_i, b_i is the body force, and $(\,)_{,j}$ denotes $\partial(\,)/\partial x_j$. The corresponding boundary conditions are

$$u_i = \bar{u}_i \qquad \text{on the essential boundary } \Gamma_u \tag{8}$$

$$t_i = \sigma_{ij} n_j = \bar{t}_i \qquad \text{on the natural boundary } \Gamma_t \tag{9}$$

where $\bar{u}_i$ and $\bar{t}_i$ are the prescribed displacements and tractions, respectively. n_j is the unit outward normal to the boundary Γ ($\Gamma = \Gamma_u + \Gamma_t$).

In the local meshless method, a local weak-form is constructed over a sub-domain Ω_s bounded by Γ_s, where Ω_s is located entirely inside the global domain Ω. Because the RBF shape functions satisfy the delta function property, the essential boundary conditions, Equation (8), can be imposed directly. Using the local weighted residual method, the generalized local weak-form of Equation (7) for a field node, *I*, can be written as

$$\int_{\Omega_s} w_I (\sigma_{ij,j} + b_i) d\Omega = 0 \tag{10}$$

where w_I is the weight function, which is constructed based on node *I*.

Integrating the first term of the left-hand side of Equation (10) by parts, we have

$$\int_{\Gamma_s} w_I \sigma_{ij} n_j d\Gamma - \int_{\Omega_s} (w_{I,j} \sigma_{ij} - w_I b_i) d\Omega = 0 \tag{11}$$

Usually the shape of the sub-domain Ω_s can be arbitrary, but it is convenient to take a circle or rectangle for a two-dimensional problem. When there is an intersection between the local boundary Γ_s and the global boundary Γ, the boundary Γ_s is usually composed of three parts (see Figure 1): the internal boundary Γ_{si}, the boundaries Γ_{su} and Γ_{st} over which the essential and natural boundary conditions are specified, respectively. Imposing the natural boundary condition, Equation (9), into Equation (11), we obtain

$$\int_{\Gamma_{si}} w_I t_i d\Gamma + \int_{\Gamma_{su}} w_I t_i d\Gamma + \int_{\Gamma_{st}} w_I \bar{t}_i d\Gamma - \int_{\Omega_s} (w_{I,j} \sigma_{ij} - w_I b_i) d\Omega = 0 \tag{12}$$

It is seen that the local weak-form is obtained by the locally weighted residual method. As a result, the choice of weight function is one of the key factors for the performance of this meshless method. Some special weight functions can be used to satisfy the required conditions [4]. In this paper, the 4th-order spline weight function [4] is used, because it has higher continuity and is easy to construct the weight function with zero value on the boundary of the local sub-domain. Then, Equation (12) can be simplified because the integration along Γ_{si} is zero.

Gauss quadrature is needed to numerically evaluate the integrations in Equation (12). As shown in Figure 1, for a field node $\mathbf{x}_I$, a local quadrature cell Ω_s is needed for the Gauss quadrature; for each Gauss quadrature point $\mathbf{x}_Q$, the meshless shape functions are constructed to obtain the integrand. Hence, for a field node $\mathbf{x}_I$, there exist three local domains:

- the local quadrature domain Ω_s (size r_s);
- the local weight (test) function domain Ω_w where $w_i \neq 0$ (size r_w);
- the local interpolation domain Ω_i for $\mathbf{x}_Q$ (size r_i).

These three local domains are arbitrary as long as the condition $r_s \leq r_w$ is satisfied. We usually use $r_s = r_w$, because it can simplify the local weak-form, Equation (12).

Substituting the displacement expression given in Equation (5) into the local weak-form Equation (12) and applying this local weak-form for all filed nodes, we have the following discretized system of equations,

$$\mathbf{KU} = \mathbf{F} \tag{13}$$

where $\mathbf{K}$ is the stiffness matrix and $\mathbf{F}$ is the force vector, i.e.

$$\mathbf{K}_I = \int_{\Omega_s} \mathbf{v}_I^T \mathbf{D}_e \mathbf{B} d\Omega - \int_{\Gamma_{si}} \mathbf{w}_I \mathbf{N} \mathbf{D}_e \mathbf{B} d\Gamma - \int_{\Gamma_{su}} \mathbf{w}_I \mathbf{N} \mathbf{D}_e \mathbf{B} d\Gamma \tag{14}$$

$$\mathbf{F}_I = \int_{\Omega_s} \mathbf{w}_I \mathbf{b} d\Omega + \int_{\Gamma_{st}} \mathbf{w}_I \bar{\mathbf{t}} \, d\Gamma \tag{15}$$

where **w**, **b** and $\bar{\mathbf{t}}$ are the weight function, body force and traction matrices, corresponding to node *I*, respectively, and

$$\mathbf{B}=\begin{bmatrix} \phi_{1,x} & 0 & \cdots & \phi_{n,x} & 0 \\ 0 & \phi_{1,y} & \cdots & 0 & \phi_{n,y} \\ \phi_{1,y} & \phi_{1,x} & \cdots & \phi_{n,y} & \phi_{n,x} \end{bmatrix} \tag{16}$$

$$\mathbf{v}_I=\begin{bmatrix} w_{I,x} & 0 \\ 0 & w_{I,y} \\ w_{I,y} & w_{I,x} \end{bmatrix} \tag{17}$$

$$\mathbf{N}=\begin{bmatrix} n_x & 0 & n_y \\ 0 & n_y & n_x \end{bmatrix} \tag{18}$$

In Equation (14), $\mathbf{D}_e$ is the effective material matrix that is obtained from the effective constitutive equation, i.e.:

$$\mathbf{D}_e(\mathbf{x}_Q)=\frac{E_e(\mathbf{x}_Q)}{1-v_e^2(\mathbf{x}_Q)}\begin{bmatrix} 1 & v_e(\mathbf{x}_Q) & 0 \\ v_e(\mathbf{x}_Q) & 1 & 0 \\ 0 & 0 & \dfrac{1-v_e^2(\mathbf{x}_Q)}{2} \end{bmatrix} \quad \text{for plane stress} \tag{19}$$

where E_e and v_e are effective Young's modulus and Poisson's ratio, which will be discussed in the following section.

It should be mentioned here that to get the matrix **K** in Equation (14), Gauss quadrature is used, and it means that **K** is obtained based on all quadrature points. Hence, $\mathbf{D}_e$ should be the material parameter matrix at the Gaussian quadrature point.

3. Determination of the effective material parameters

3.1 Effective material parameters

The strain-stress relationship can be taken in the form [29]

$$\varepsilon_{ij} = f(\sigma_{ij}) \tag{20}$$

where f is a function and ε_{ij} is the total strain tensor, which is the summation of conservative elastic ε_{ij}^{e} and nonconservative plastic part ε_{ij}^{p}, i.e.,

$$\varepsilon_{ij} = \varepsilon_{ij}^{e} + \varepsilon_{ij}^{p} \tag{21}$$

The elastic strain tensor is related to the stress tensor and is given by Hooke's law for isotropic material as [30]

$$\varepsilon_{ij}^{e} = \frac{1+\nu}{E}\sigma_{ij} - \frac{\nu}{E}\sigma_{kk}\delta_{ij} \tag{22}$$

where δ_{ij} is the Delta function.

The plastic strain tensor is related to the deviatoric part of stress tensor and is given by Hencky's total deformation relation

$$\varepsilon_{ij}^{p} = \Psi S_{ij} \tag{23}$$

where Ψ is a scalar valued function, given by

$$\Psi = \frac{3\varepsilon_{\text{equivalent}}^{p}}{2\sigma_{\text{equivalent}}} = \frac{3}{2}\frac{\sqrt{2\varepsilon_{ij}^{p}\varepsilon_{ij}^{p}/3}}{\sqrt{3S_{ij}S_{ij}/2}} \tag{24}$$

and

$$S_{ij} = \sigma_{ij} - \frac{1}{3}\sigma_{kk}\delta_{ij} \tag{25}$$

Substituting Equations (22)~(25) into Equation (21), we can get

$$\begin{aligned}
\varepsilon_{ij} &= \varepsilon_{ij}^{e} + \varepsilon_{ij}^{p} \\
&= \frac{1+\nu}{E}\sigma_{ij} - \frac{\nu}{E}\sigma_{kk}\delta_{ij} + \Psi S_{ij} \\
&= \frac{1+\nu}{E}\sigma_{ij} - \frac{\nu}{E}\sigma_{kk}\delta_{ij} + \Psi\left(\sigma_{ij} - \frac{1}{3}\sigma_{kk}\delta_{ij}\right) \\
&= \left(\frac{1+\nu}{E} + \Psi\right)\sigma_{ij} - \left(\frac{\nu}{E} + \frac{1}{3}\Psi\right)\sigma_{kk}\delta_{ij}
\end{aligned} \tag{26}$$

Equation (26) can be re-written as

$$\varepsilon_{ij} = \left(\frac{1+\nu_e}{E_e}\right)\sigma_{ij} - \left(\frac{\nu_e}{E_e}\right)\sigma_{kk}\delta_{ij} \tag{27}$$

where E_e and ν_e are the equivalent Young's modulus and Poisson's ratio, which are given by

$$E_e = \frac{1}{\frac{1}{E} + \frac{2\Psi}{3}} \tag{28}$$

$$\nu_e = \frac{\frac{\nu}{E} + \frac{\Psi}{3}}{\frac{1}{E} + \frac{2\Psi}{3}} \tag{29}$$

Equation (27) is the effective constitutive equation for the analysis of material nonlinearity.

For example, for the elastic-perfectly plastic material, as shown in Figure 2, the yield stress is σ_0. Using Equations (28) and (29), we can obtain the effective material parameters

$$\frac{1}{E_e^{\text{perfect}}} = \frac{1}{E} + \frac{\varepsilon^p}{\sigma_0}, \quad \nu_e^{\text{perfect}} = E_e^{\text{perfect}}\left(\frac{\nu}{E} + \frac{\varepsilon^p}{\sigma_0}\right) \tag{30}$$

For the linear work-hardening materials, as shown in Figure 3, the yield stress is σ_0 and the tangent modulus is E_T. Using Equations (28) and (29), we can obtain the effective material parameters

$$\frac{1}{E_e^{\text{harden}}} = \frac{\sigma_0}{E\sigma} + \frac{\sigma - \sigma_0}{\sigma E_T}, \ \nu_{\text{e}}^{\text{harden}} = E_e^{\text{harden}}\left(\frac{\nu}{E} + \frac{\sigma_0 - \sigma}{2\sigma}\left(\frac{1}{E} - \frac{1}{E_T}\right)\right) \tag{31}$$

It should be mentioned here that the effective material parameters are functions of the final state of stress fields. They are also related to the position of a point because the stress is also the function of position. Hence, the effective material parameters can be thought to be field variables describing the material properties of each point, where the stress state is unique. As discussed in Section 2.2, the system of equations is constructed based on the Gauss quadrature points, and therefore, the effective material parameters should be also calculated for Gauss quadrature points.

3.2 The projection technique

To get solution from Equation (13), the effective material matrix $\mathbf{D}_e$ in Equation (19) should be calculated at first. However, as discussed above, the effective material parameters are functions of the final stress fields, which are usually unknown. Hence, the direct method is impossible to get the final solution, and the following iteration method based on the projection technique [29] is used.

a) the initial linear elastic analysis

First, a linear elastic analysis is carried out to get the initial stress field. To determine whether a material enters the plastic range, the Von Mises yield criterion [26], which compares the equivalent stress with the yield stress, is used. If the equivalent stress calculated from linear analysis is smaller than the yield stress, σ_0, the computing is finished because the material still satisfies the linear elasticity; if the equivalent stress is larger than the yield stress, it means the deformation already enters the plastic region, and the following iteration computing will be performed.

b) the iteration computing based on the projection technique

From the initial linear elastic analysis, we get Point 1 as shown in Figure 4. The strain value is kept unchanged (i.e. strain controlled), and Point 1 is projected on the experimental uniaixial $\sigma - \varepsilon$ curve to get Point $1'$. The effective value of Young's modulus, $E_e^{(1)}$, for the next iteration is obtained from the slope of the straight line 0-$1'$, and then the effective Poisson's ratio, $v_e^{(1)}$, can also be obtained from Equation (29). Using the new effective materials parameters $E_e^{(1)}$ and $v_e^{(1)}$, the next linear elastic meshless analysis is carried out to get Point 2 and its projection Point $2'$, and further to obtain $E_e^{(2)}$ and $v_e^{(2)}$ similarly. This iterative procedure is repeated and meshless elastic analysis with currently evaluated $E_e^{(k)}$ and $v_e^{(k)}$ is performed until all the effective material parameters converge and

equivalent stress falls on the experimental uniaxial stress-strain curve. However, if the applied loading is too large, the computing may not converge, and it means that the material is already failure, and this certain loading is called the critical failure loading which is also an important parameter for solids and structures.

Table 1 The flowchart of the pseudo-elastic LRPIM method

1. Input geometry, material properties, external forces, boundary conditions, etc.;
2. Construct local quadrature domains for field nodes;
3. Compute meshless shape functions for each Gauss point;
4. Form initial $\mathbf{K}_{(0)}$ based on the linear elastic analysis;
5. Solve $\mathbf{K}_{(0)}\mathbf{u} = \mathbf{F}$ and get stress for all quadrature points;
6. Compare equivalent stress $\sigma_{e\,(\mathbf{x}_Q)}$ with the yield stress, σ_0,
   If $\sigma_e(\mathbf{x}_Q) \le \sigma_0$ stop computing; output results; go to 7;
   - 6.1 Calculate initial error R for $E_e^{(0)}$ and $E_e^{(1)}$;
   - 6.2 Loop while ($R \ge$ tolerance and the iteration number $\le$ the given number)
     - 6.2.1 Calculate $E_e^{(i+1)}$ and $\nu_e^{(i+1)}$ using the projection technique;
     - 6.2.2 Update $\mathbf{D}_e$ and form $\mathbf{K}_{(i+1)}$;
     - 6.2.3 Solve $\mathbf{K}_{(i+1)}\mathbf{u}_{(i+1)} = \mathbf{F}$;
     - 6.2.4 Calculate stress and the equivalent stress $\sigma_e^{(i+1)}$;
     - 6.2.5 Calculate error R for $E_e^{(i)}$ and $E_e^{(i+1)}$
     - 6.2.6 End loop 6.2.
   - 6.3 If the iteration number > the given number,
     then this problem does not converge, report failure and go to 7;
   - 6.4 Output results.
7. End

Table 1 lists the flowchart of the pseudo-elastic LRPIM for the material nonlinear analysis. From this flowchart, it can be found that an iteration technique is used to get the convergent results, and the Newton-Raphson iteration method is employed in this paper. The iteration criteria is defined as

$$\sqrt{\frac{\sum_{j=1}^{n}(E_{ej}^{(i+1)} - E_{ej}^{(i)})^2}{\sum_{j=1}^{n}(E_{ej}^{(i)})^2}} \le R \tag{32}$$

where n is the number of quadrature points, $E_e^{(i)}$ and $E_e^{(i+1)}$ are the effective Young's modulus of the ith and the $(i+1)$th iteration steps, respectively, and R is a specified accuracy tolerance.

4. Numerical examples

To illustrate the effectiveness of the presented pseudo-elastic LRPIM formulation for the material nonlinear problems, several cases are studied. The units are taken as standard international (SI) units, unless mentioned otherwise. Sixteen field nodes, which are the closest to the interpolation point, are used to construct the meshless RBF shape functions.

4.1 Uniaxial tension of a bar

Figure 5(a) shows a 3 m×0.3 m cantilever bar is subjected to a uniform tensile pressure having a resultant F. The Young's modulus is assumed as $E = 2.1\times10^{11}$ Pa, the Poisson's ratio is $\nu = 0.3$, and the yield stress is $\sigma_0 = 1.68\times10^8$ Pa. The bar is assumed as being in a plane stress state. As shown in Figure 5(b), 163 irregularly distributed field nodes are used to discretize the problem domain.

The material is initially considered as elastic-perfectly plastic. The present pseudo-elastic LRPIM method is applied to get the results. Figures 6 and 7 show the convergence paths for different F. It can be seen that the present pseudo-elastic LRPIM method using the projection technique can quickly produce convergent results. However, the number of iteration steps will increase as F increases. When F is larger than a certain value, the results will become non-convergent, and the structure fails, as shown in Figure 8. This value is called the critical failure load, and it is $F = 55.5\times10^6$ N in this problem.

Figure 9 shows the displacement u_x of the free end in the x-direction under different loadings. For comparison, FEM results [31] are also plotted in the same figure. It can be seen that the results of the present method are in good agreement with the FEM results. It should

be mentioned that the present method needs much less iteration steps and therefore, is more efficient. For comparison, the thin-plate spline (TPS) RBF is also used to construct the meshless shape functions. It has been found that the TPS leads to slightly worse accuracy than the MQ. However, the TPS RBF does not involve undetermined parameter.

A work-hardening material is also considered, as shown in Figure 10. It clearly shows that the pseudo-elastic LRPIM method also gives convergent results for $F = 80\times10^6$ N. A work-hardening material has a much higher critical failure load than an elastic-perfectly plastic material.

4.2 A V-notch plate

A V-notch plate, subjected to the axial load *F* is considered, as shown in Figure 11. The plate has a length of $L = 40$ mm and a width of $d = 20$ mm; the notch has a width of $a = 10$ mm, and the depth of $b = 2.5$ mm. The material is elastic-perfectly plastic, having Young's modulus of $E = 1.0\times10^8$ Pa, Poisson's ratio of $\nu = 0.2$, and a yield stress of $\sigma_0 = 3.0\times10^7$ Pa. Irregularly distributed 431 field nodes are used.

Figure 12 presents the distribution of stress σ_{xx} along *y*, in the cross-section of x=0, for *F*=1880 N. It clearly shows that there is a stress concentration at the tip of the notch. For comparison, the FEM results are also plotted in the same figure. It can be observed that the results obtained by the present method are in a very good agreement with the FEM results. In addition, the critical failure load of 2286 N, obtained by the present method, is comparable with the analytical result of 2250 N [32].

4.3 A thick cylinder subjected to internal pressure

A cylindrical vessel [31] , subjected to an internal pressure *p* is considered, as shown in Figure 13. It is under plane strain condition. Due to symmetry, only a quarter of the cylinder is modeled, using 163 irregularly distributed field nodes, as shown in Figure 14. The

Young's modulus is $E = 2.1\times10^{11}$ Pa, the Poisson's ratio is $\nu = 0.3$, and the yield stress is $\sigma_0 = 2.4\times10^{8}$ Pa. An elastic-perfectly plastic material is considered.

Figure 15 presents the displacements obtained by the present pseudo-elastic LRPIM method, and the analytical results [26] are also plotted in the same figure for comparison. It is obvious that the LRPIM method gives very accurate results.

5. Conclusions

In the present paper, a meshless pseudo-elastic LRPIM formulation is developed for solving elasto-plastic problems. The local Petrov-Galerkin weak-form is used to get the meshless system of equations, and the radial basis interpolation is used to construct the meshless shape function. The Hencky's total deformation theory is utilized to define the effective material parameters, which are treated as spatial field variables and considered to be functions of final stress state and material properties. These effective material parameters are obtained in an iterative manner using strain controlled projection method. Examples are presented to illustrate the effectiveness of the present formulation for the elasto-plastic analysis of solids. It has been found that the new formulation leads to convergent and accurate results, if the applied loading is smaller than the critical failure loading. In addition, the present method can also accurately give the critical failure loading. In summary, the studied examples have demonstrated that the present pseudo-elastic LRPIM method is very effective for the analysis of nonlinear materials with proportional loading.

ACKNOWLEDGEMENT

The authors gratefully acknowledge the kind help from Dr. T. Dr. Vodenitcharova.

References

[1] Belytschko T, Liu WK, Moran B. Nonlinear finite elements for continua and structures. John Wiley & Sons, 2000.

[2] Zienkiewicz OC, Taylor RL. The finite element method (5th ed.). Butterworth Heinemann, Oxford, 2000.

[3] Liu GR. Mesh Free Methods: Moving Beyond the Finite Element Method. CRC press, USA, 2002.

[4] Liu GR, Gu YT. An introduction to meshfree methods and their programming. Springer Press, Berlin, 2005.

[5] Gingold RA, Moraghan JJ. Smooth particle hydrodynamics: theory and applications to non spherical stars. Monthly Notices of the Royal Astronomical Society 1977; 181, 375-389.

[6] Zhang X, Song KZ, Lu MW, Liu X. Meshless methods based on collocation with radial basis functions. Computational Mechanics 2000; 26(4): 333-343.

[7] Liu Y, Liew KM, Hon YC, et al. Numerical simulation and analysis of an electroactuated beam using a radial basis function.Smart Materials & Structures, 14 (6): 1163-1171, 2005.

[8] Nayroles B, Touzot G, Villon P. Generalizing the finite element method: diffuse approximation and diffuse elements. Computational Mechanics 1992; 10, 307-318.

[9] Belytschko T, Lu YY, Gu L. Element-Free Galerkin Methods. International Journal for Numerical Methods in Engineering 1994; 37:229-256.

[10] Liu WK, Jun S, Zhang Y. Reproducing kernel particle methods. International Journal for Numerical Methods in Engineering 1995; 20: 1081-1106.

[11] Liu GR, Gu YT. A point interpolation method for two-dimensional solids. International Journal for Numerical Methods in Engineering 2001; 50: 937-951.

[12] Gu YT, Liu GR. A boundary radial point interpolation method (BRPIM) for 2-D structural analyses. Structural Engineering and Mechanics, An International Journal 2003; 15(5): 535-550.

[13] Gu YT, Liu GR. Hybrid boundary point interpolation methods and their coupling with the element free Galerkin method. Engineering Analysis with Boundary Elements 2003; 27(9): 905-917.

[14] Atluri SN, Zhu T. A new meshless local Petrov-Galerkin (MLPG) approach in computational mechanics. Computational Mechanics 1998; 22: 117-127.

[15] Atluri SN, Kim HG, Cho JY. A critical assessment of the truly meshless local Petrov-Galerkin (MLPG), and Local Boundary Integral Equation (LBIE) methods. Computational Mechanics 1999; 24:348-372.

[16] Gu YT, Liu GR, A meshless local Petrov-Galerkin (MLPG) method for free and forced vibration analyses for solids, Computational Mechanics 2001; 27 (3): 188-198.

[17] Gu YT; Liu GR. A local point interpolation method for static and dynamic analysis of thin beams, Computer Methods in Applied Mechanics and Engineering 2001; 190: 5515-5528.

[18] Liu GR, Gu YT. A local radial point interpolation method (LR-PIM) for free vibration analyses of 2-D solids. Journal of Sound and Vibration 2001; 246(1): 29-46.

[19] Liu GR, Gu YT. Comparisons of two meshfree local point interpolation methods for structural analyses. Computational Mechanics 2002; 29(2): 107-121.

[20] Xiao JR, McCarthy MA. Meshless analysis of the obstacle problem for beams by the MLPG method and subdomain variational formulations. European J. of Mechanics A-Solids 2003; 22 (3): 385-399.

[21] Xiao JR, Gama BA, Gillespie JW, Kansa EJ. Meshless solutions of 2D contact problems by subdomain variational inequality and MLPG method with radial basis functions. Engineering Analysis with Boundary Elements 2005; 29 (2): 95-106.

[22] Wang QX, Lam KY, Li H and Gu YT. Analysis of microelectromechanical systems (MEMS) by meshless Local Kriging (LoKriging) method. Journal of Chinese Institute of Engineers 2003; 27 (4): 573-583.

[23] Liu Y., Hon Y.C. and Liew K.M., A meshless Hermite-type radial point interpolation method for Kirchhoff plate problems. International Journal for Numerical Method in Engineering, Vol. 66, 1153-1178, 2006

[24] Hon YC, Lu MW, Xue MW and Zhou X, Numerical algorithm for triphasic model of charged and hydrated soft tissues, Computational Mechanics, Vol. 29, Isssue 1, 1-15, 2002.

[25] Marcal PV, King IP. Elastic Plastic Analysis of Two-Dimensional Stress Systems by the F.E.M. Int. J. Mech. Sci. 1967; 9: 143–155.

[26] Owen DRJ, Hinton E. Finite Elements in Plasticity: Theory and Practice, Pineridge Press Limited, 1980.

[27] Seshadri R. The Generalized Local Stress-Strain ~GLOSS Analysis—Theory and Applications. ASME J. Pressure Vessel Technol 1991; 113: 219–227.

[28] Babu S, Iyer PK. Inelastic Analysis of Components Using a Modulus Adjustment Scheme. ASME J. Pressure Vessel Technology 1998; 120: 1–5.

[29] Desikn V and Sethuraman R. Analysis of Material Nonlinear Problems Using Pseudo-Elastic Finite Element Method. Journal of Pressure Vessel Technology 2000; 122: 457-461.

[30] Timoshenko SP, Goodier JN. Theory of Elasticity, 3rd Edition. McGraw-hill, New York, 1970.

[31] Liew KM, Wu YC, Zou GP, Ng TY. Elasto-plasticity revisited: numerical analysis via reproducing kernel particle method and parametric quadratic programming. Int. J. Numer. Meth. Engng 2002; 55:669–683.

[32] Song KZ, Zhang X, Lu MW. Elasto-plastic analysis based on collocation with moving least square method. Acta Mechanica Solida Sinica, 16(2): 162-170, 2003.

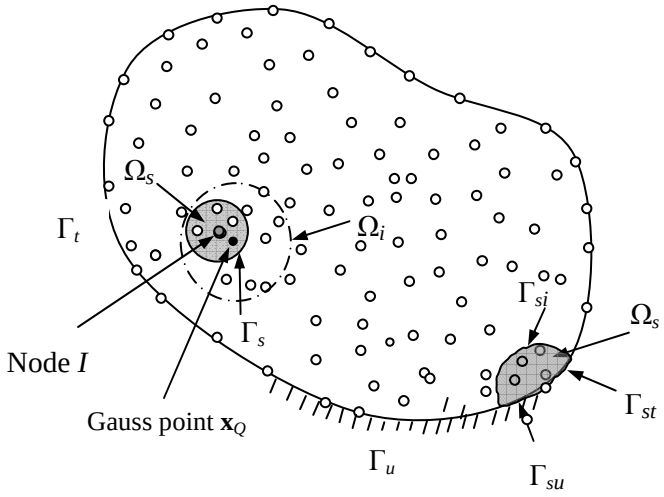

Figure 1 Local domains used in the pseudo-elastic LRPIM

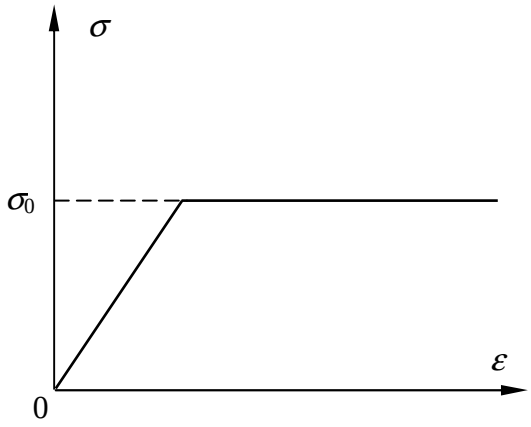

Figure 2 The stress-strain relation for a elastic-perfectly plastic material

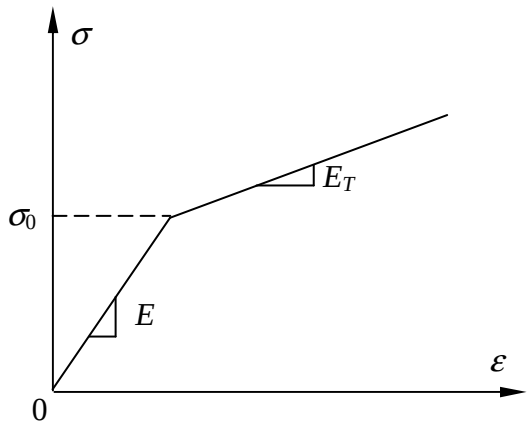

Figure 3 The stress-strain relation for a linear work-hardening material

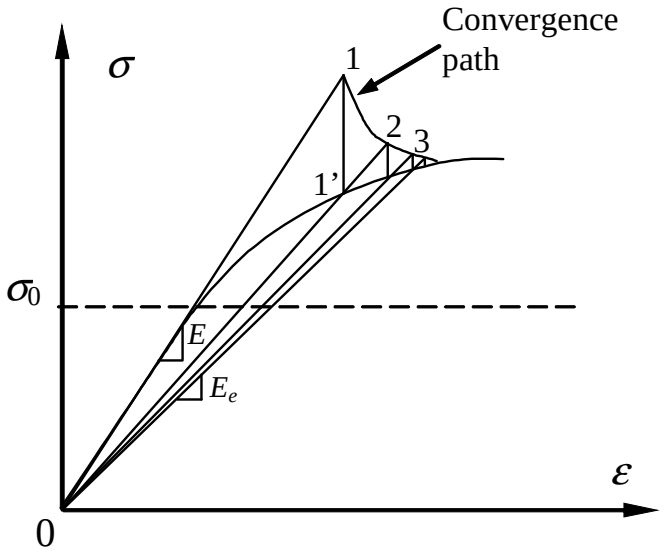

Figure 4 To determination E_e by the projection method

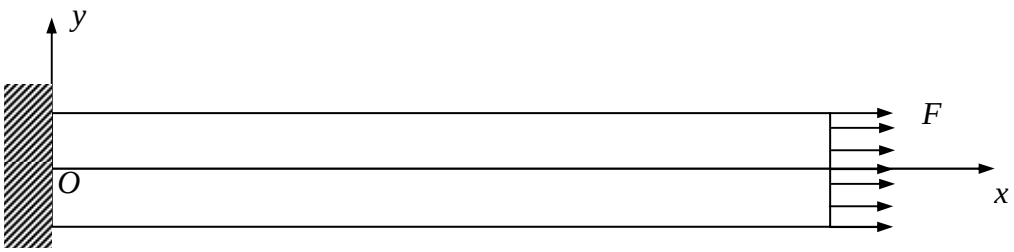

(a) The cantilever bar

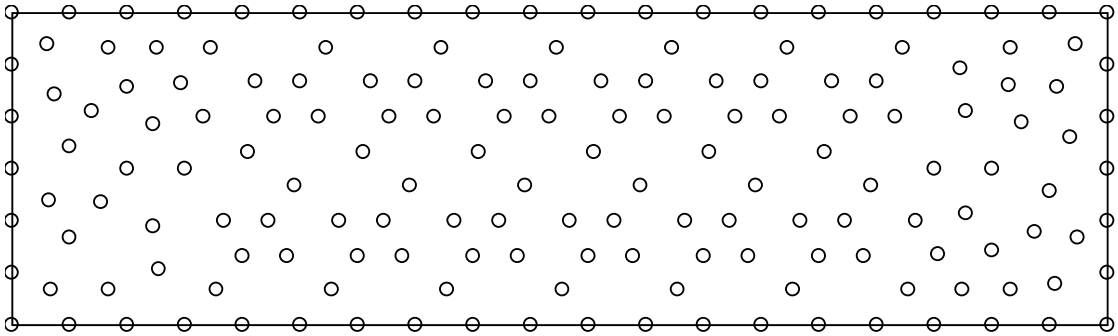

(b) 143 irregular field nodes

Figure 5 A cantilever bar under uniaxial tension

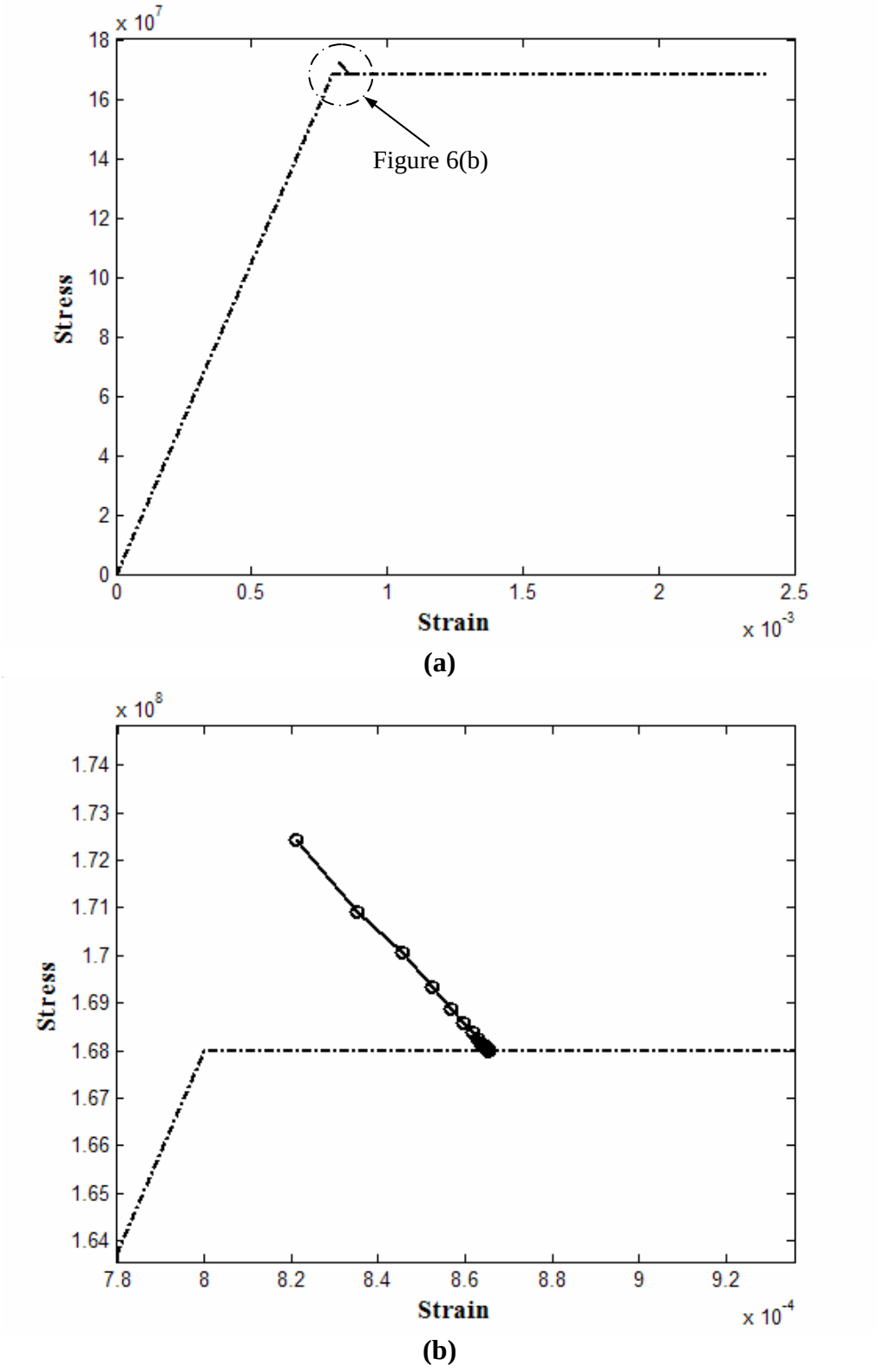

Figure 6 The convergence path for the bar with the elastic-perfectly plastic material (F=54MN); (a) the convergence path; (b) the magnified convergence path

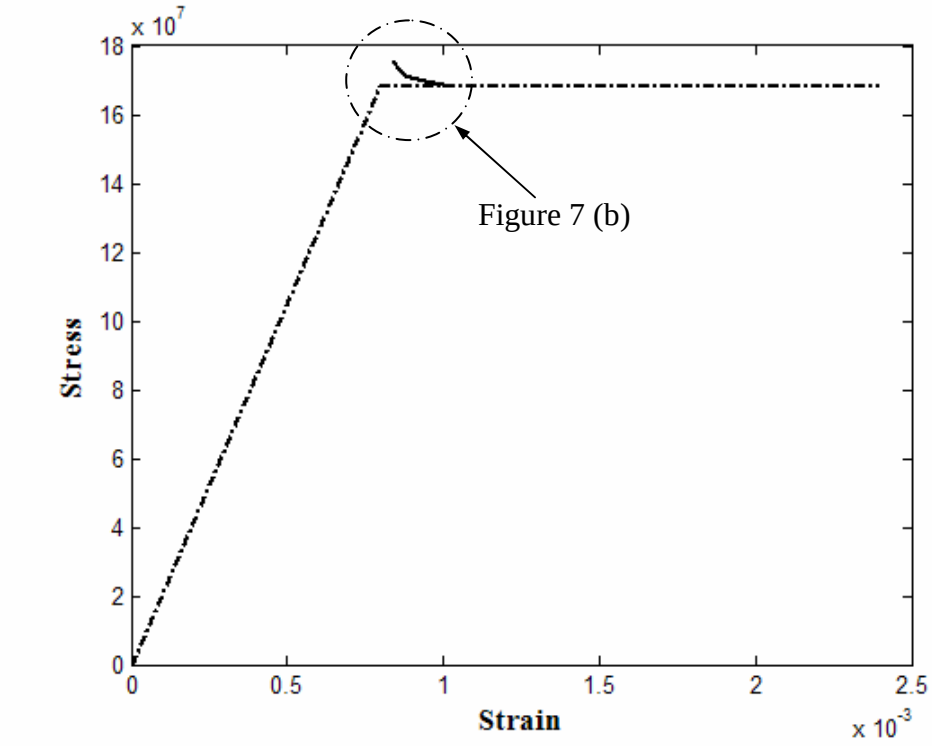

(a)

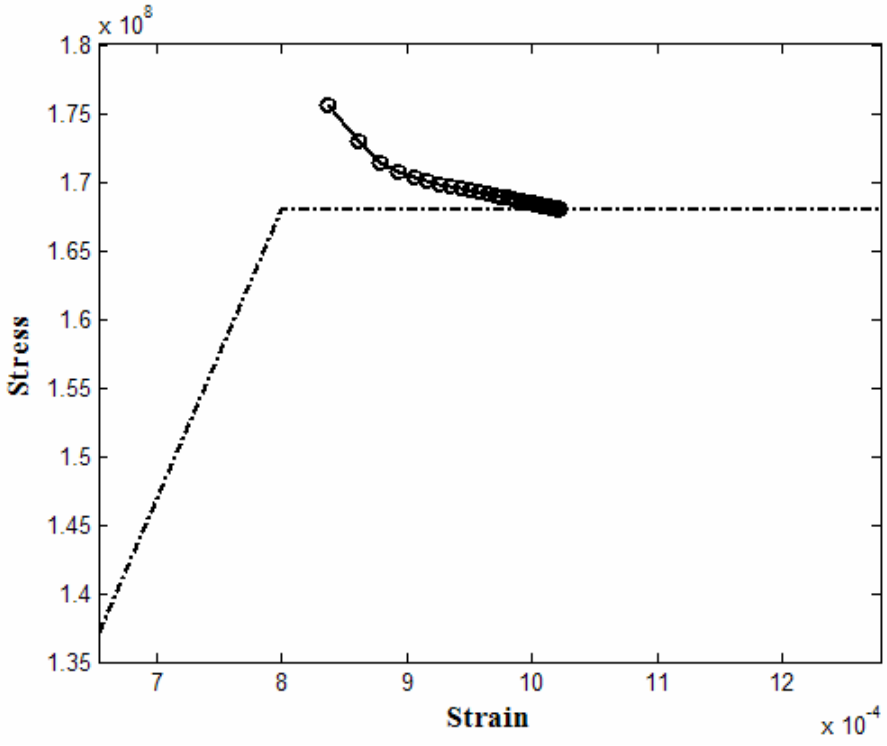

(b)

Figure 7 The convergence path for the bar with the elastic-perfectly plastic material (F=55MN); (a) the convergence path; (b) the magnified convergence path

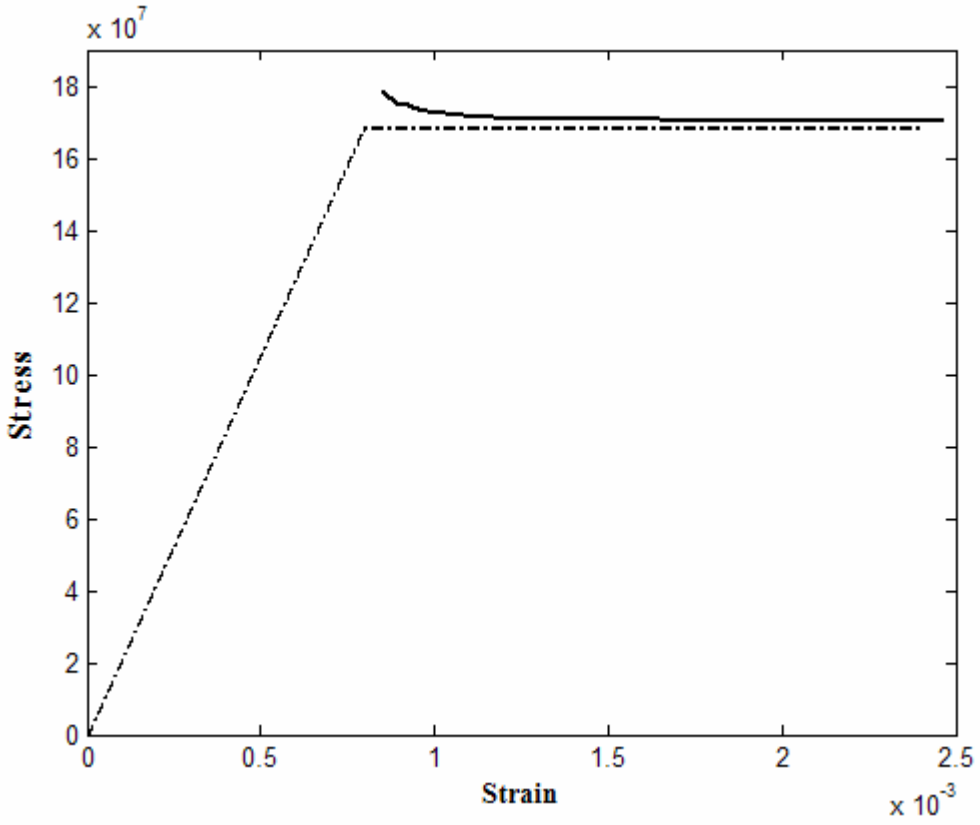

Figure 8 The convergence path for the bar with the elastic-perfectly plastic material (F=56MN)

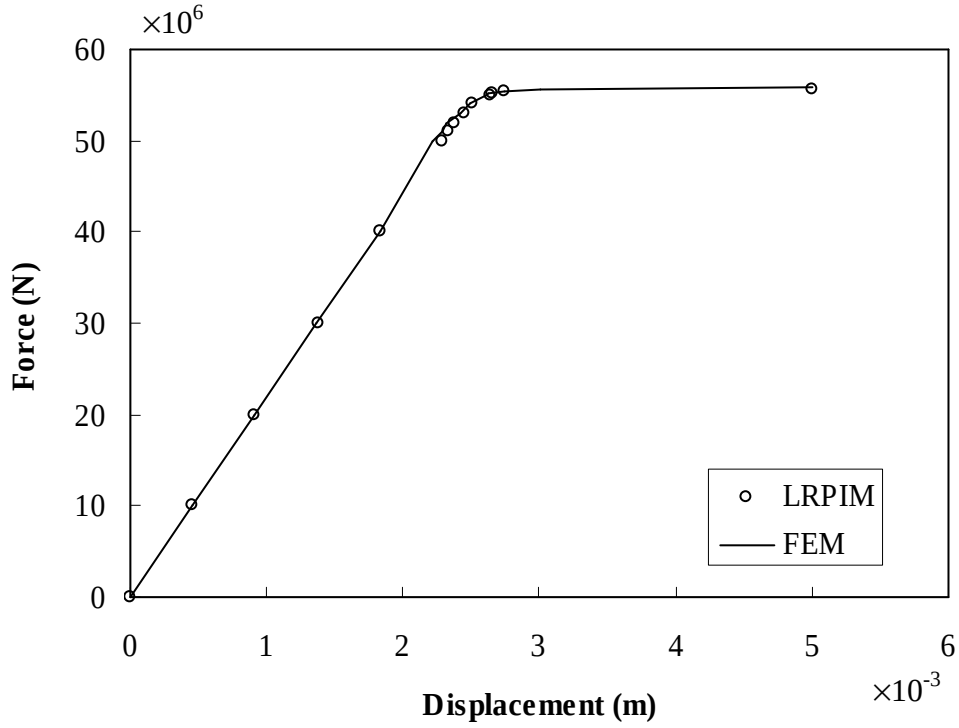

Figure 9 The displacement-force response for the bar with the elastic-perfectly plastic material

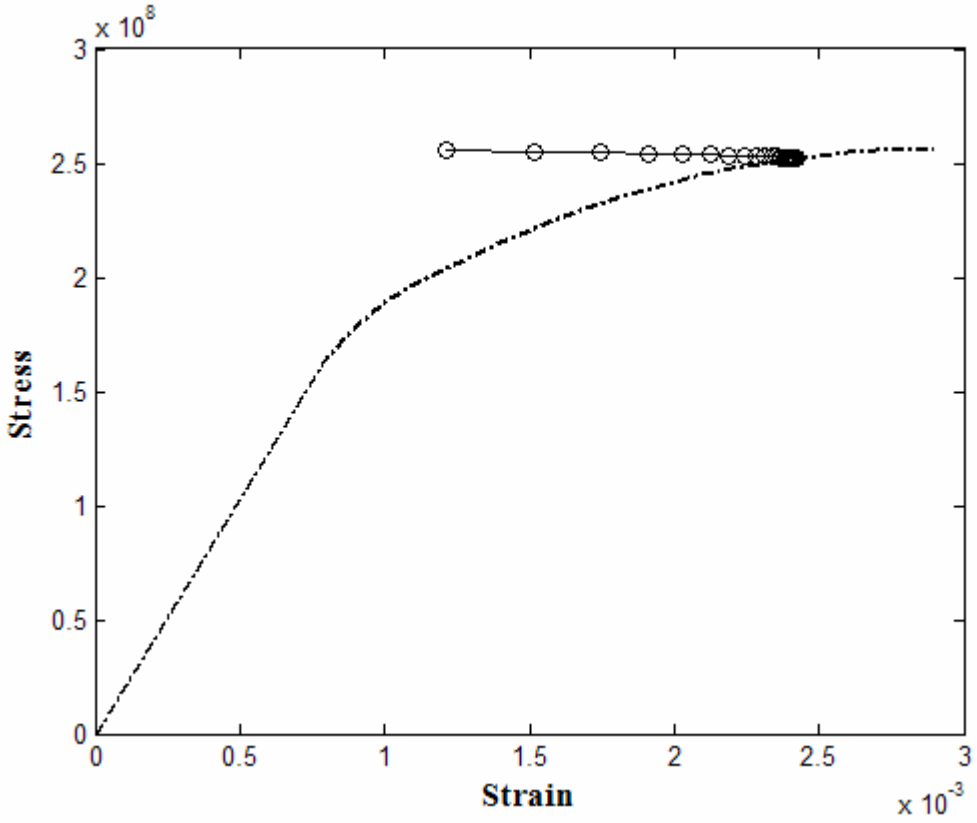

Figure 10 The convergence path for the bar with the work-hardening material (*F*=80MN)

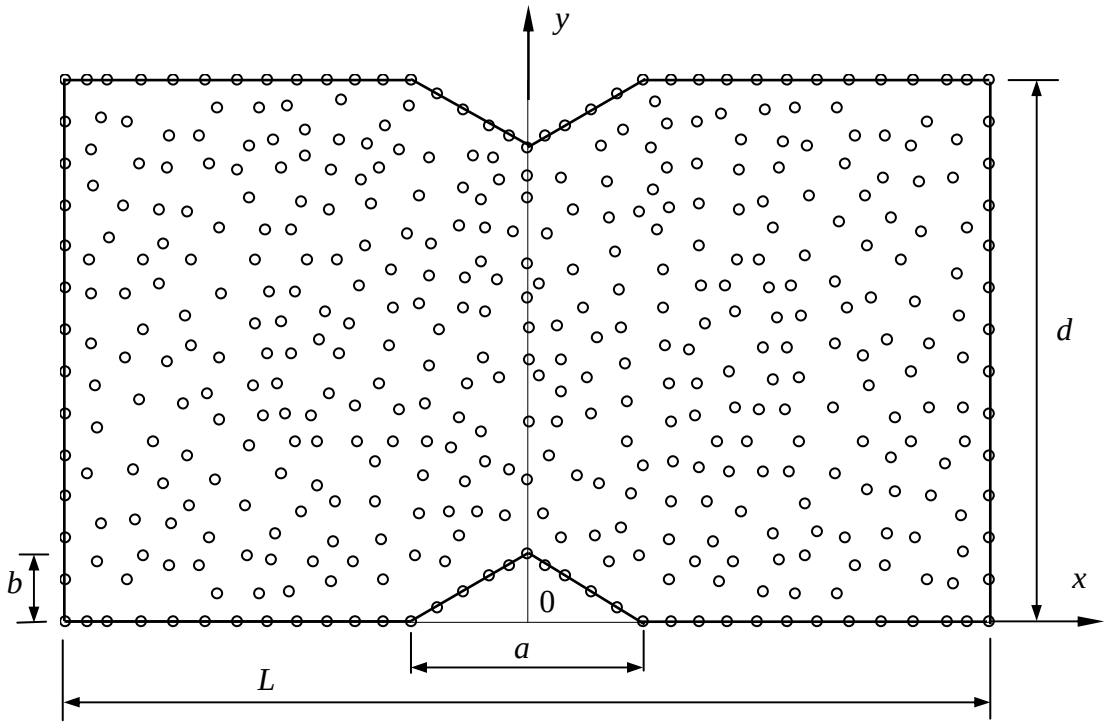

Figure 11 The nodal distribution for a V-notched plate

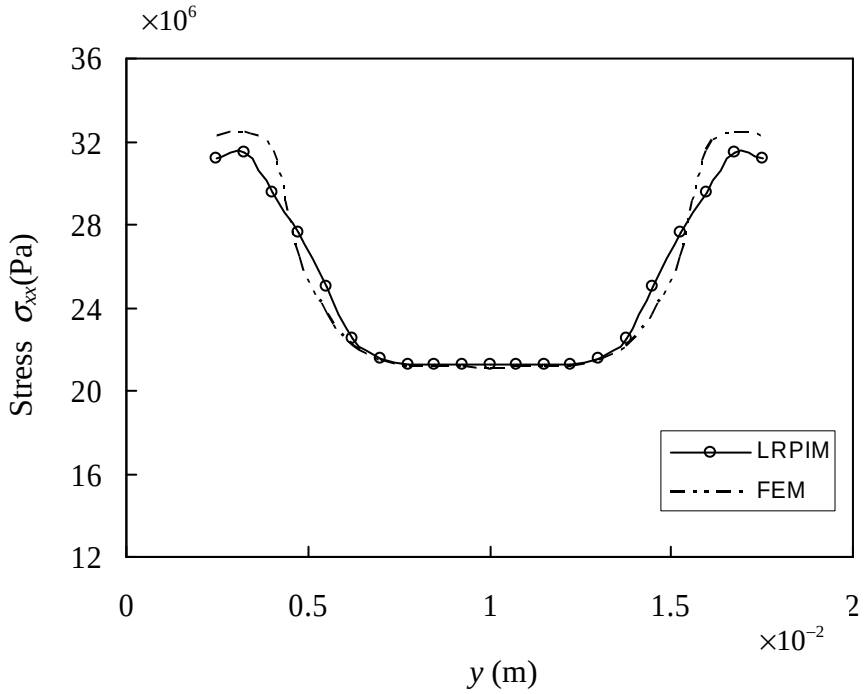

Figure 12 The distribution of stress, σ_{xx}, along the cross-section of x=0 for the V-notch problem

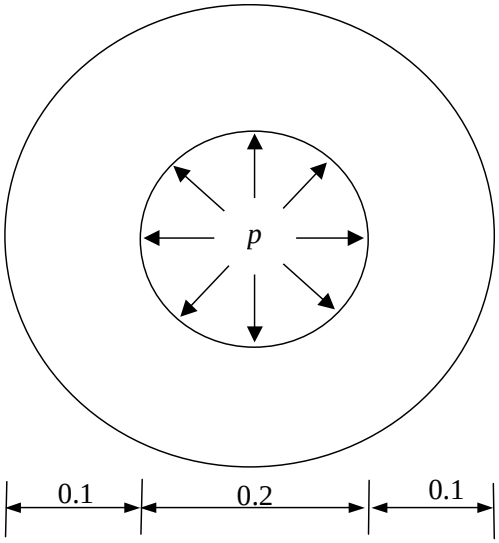

Figure 13 Hollow cylinder subjected to internal pressure

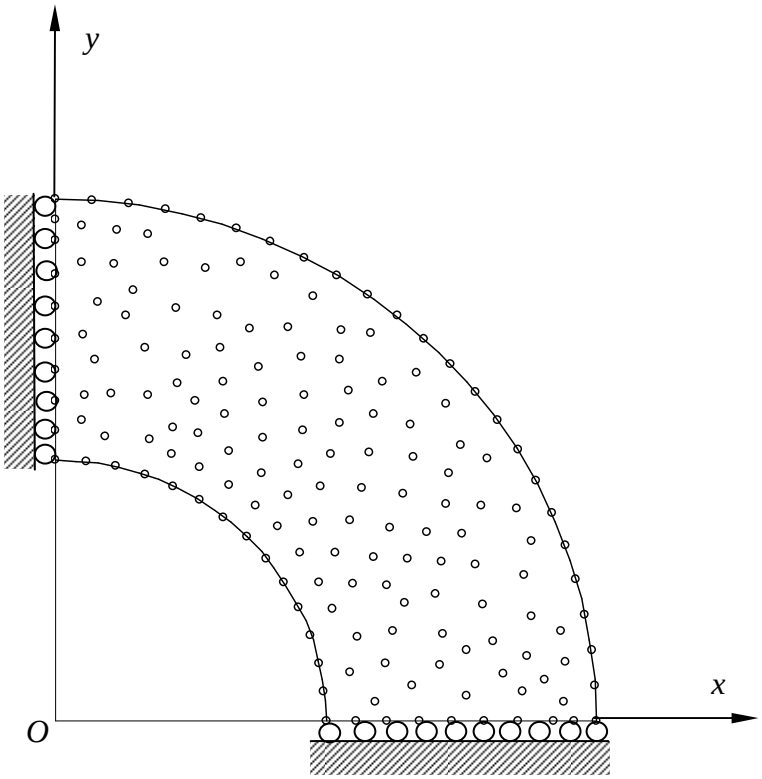

Figure 14 The nodal distribution of the hollow cylinder

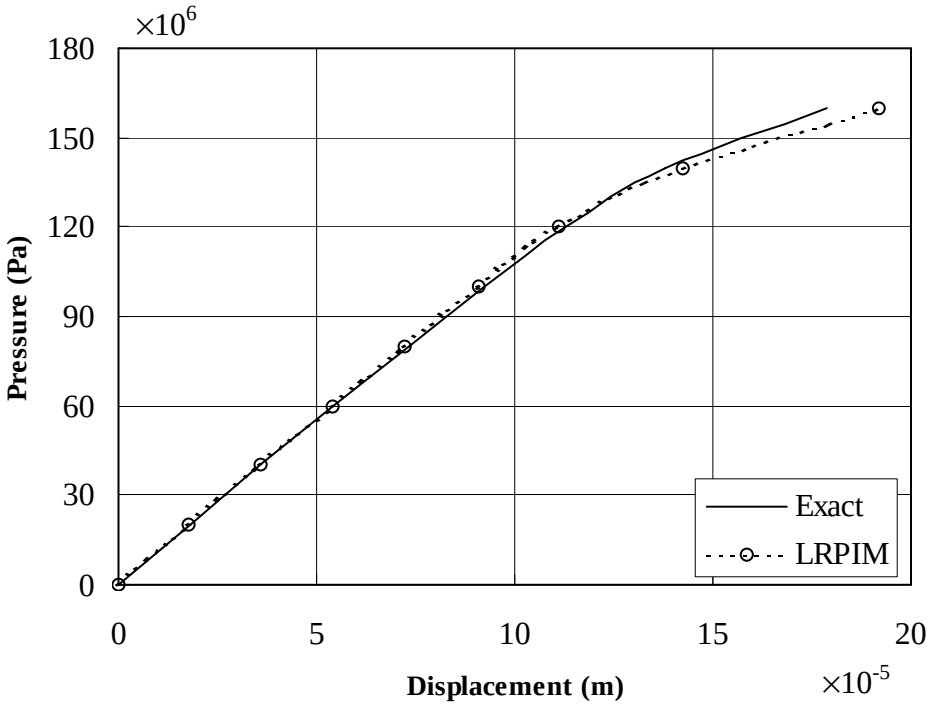

Figure 15 The radial displacement at inner surface vs. the pressure